AIAA-2026-4378

Controlled Distortion and Recovery in an Aggressive, Modular Diffuser

Joshua W. Fletcher[1], Sean Wang [2], Bojan Vukasinovic[3], James Mace[4], and Ari Glezer[5]
Woodruff School of Mechanical Engineering, Georgia Institute of Technology, Atlanta, GA, USA
Mory Mani[6]
Massachusetts Institute of Technology, Cambridge, MA, USA
Zachary T. Stratton[7] and John T. Spyropoulos[8]
Naval Air Warfare Center – Aircraft Division, Patuxent River, MD, USA

Massively separated flow along each of the diverging surfaces of a short, high aspect ratio (AR = 6) rectangular-to-circular diffuser section, downstream of a bend and upstream of the AIP of an inlet system, is mitigated (up to $M \approx 0.5$) in joint experimental/numerical investigations with significant improvement of the total pressure distribution at the AIP. The flow separation along each surface of the diffuser, coupled with the Dean circulations of the bend, gives rise to two pairs of counter-rotating vortices at the AIP. Separation is mitigated using a jet array module along each of the long sides of the diffuser's rectangular inlet downstream of the bend. Each control module comprises a spanwise array of yawed surface jets on each side of the inlet plane that gives rise to surface-bound streamwise vortices having an opposite sense of rotation to vorticity along the surface at which they issue. Initially, these control vortices interact destructively with the opposite upstream vorticity in the base flow and suppress its spanwise accumulation. Subsequently, control-induced vortices coalesce into larger-scale, counter-rotating vorticity concentrations that advect the near-surface flow away from the central plane and cut off the surface vorticity that feeds the central vortex pair of the base flow. The present investigations show that fluidic actuation leads to cross stream spreading of the high aspect ratio core flow towards the diverging surfaces and ultimate reattachment that leads to reasonably axisymmetric distribution of total pressure at the AIP with reductions of 50-70% in circumferential total pressure distortion $DPCP_{avg}$. Moreover, control of the total pressure at AIP significantly reduces all aeromechanical excitation indices up to the fourth (relevant) order.

---

[1] Graduate Research Assistant, AIAA Member
[2] Graduate Research Assistant, AIAA Member
[3] Senior Research Engineer, AIAA Member
[4] Consultant, AIAA Member
[5] Professor, AIAA Fellow
[6] Consultant, AIAA Member
[7] Aerospace Engineer, NAWCAD, AIAA Member
[8] Aerospace Engineer - Lead for Inlets, Nozzles, and Aeroacoustics, NAWCAD, AIAA Associate Fellow

Nomenclature

AFC	=	Active flow control
AIP	=	Aerodynamic interface plane
AR	=	Inlet/channel aspect ratio
C_q	=	Jet mass flow rate coefficient
C_μ	=	Jet momentum coefficient
D_{AIP}	=	AIP diameter
$DPCP_{avg}$	=	Average circumferential distortion descriptor
$DPRP_{max}$	=	Maximum radial distortion descriptor
L	=	throat-to-AIP length
r	=	Radius of curvature at the bend
r/D	=	Radius of curvature at the bend normalized by AIP diameter
M	=	Mach number
M_{AIP}	=	Mach number at the aerodynamic interface plane
θ	=	Bend turning angle
ω	=	Vorticity

I. Introduction

Advanced aircraft propulsion systems feature streamlined airframe integration and highlight the need for increasingly complex offset inlet designs. These offset inlets allow for greater freedom of airframe design, and potential drag and performance improvements. However, offset diffusers have adverse internal flow characteristics and pose a significant design challenge. Without appropriate flow management techniques, high turning angles and changes in cross-sectional areas can cause significant total pressure losses as well as distortion at the Aerodynamic Interface Plane (AIP), leading to detrimental aeromechanical interactions with the downstream compressor fan blades, compromising turbomachinery operability and performance.

High-speed subsonic flows within offset inlets are dominated by flow structures that can lead to performance losses at the AIP. Connolly et al. [1] simulated the flow through a serpentine diffuser with a rectangular cross section and found that the secondary flows were driven by a pair of counter-rotating streamwise vortices known as Dean vortices [2]. These vortices form in curved pipes and channels due to the competing effects of the outward-directed centrifugal force that dominates in the center of the bend, and the inward-directed pressure gradient that dominates in the lower momentum boundary layer. Additionally, significant turning of the diffuser's centerline or curvature along the surface due to changes in cross-sectional area can lead to adverse pressure gradients, leading to flow separation and the formation of streamwise vortices [3,4]. Burrows et al. also found that at high enough Mach numbers, the local flow acceleration due to separation can even cause transonic shocks to form in the diffuser bend [5]. These factors worsen the diffuser performance and lead to total pressure losses and total-pressure distortion at the AIP.

To target these detrimental flow structures, passive and active flow control techniques have been developed and investigated to reduce the adverse effects of integrated inlet flow on propulsion system performance. Passive vortex generators have been used to improve recovery and reduce distortion by affecting the evolution of secondary flow vortices [6] and partially suppressing internal separation [7-9]. While these passive techniques have had varying successes, they present disadvantages compared to active flow control (AFC) as their presence leads to drag and total pressure losses through the inlet, and their passive nature means they are unable to vary and adapt to changing flow conditions. To this end, many AFC approaches have been designed and tested. Scribben et al. [10] used microjets in a serpentine diffuser to reduce distortion by 70% and improve total pressure recovery by 2% at an AIP Mach number of 0.55 and jet mass flow rate coefficient C_q =0.01. Anderson et al. [11] numerically investigated a redesigned M2129 inlet S-duct and used optimized microjets to reduce DC60 (lowest pressure in 60º sector) distortion parameter below 0.1 with $C_q = 0.005$. Gartner and Amitay [12] used pulsed jets, sweeping jets, and a blowing slot to improve total pressure recovery in a rectangular diffuser, and showed that the slot-jet was less effective than pulsed or sweeping jets. Rabe [13] evaluated microjets in a double-offset diffuser driven by a gas-turbine engine and, with the jets driven by engine bleed at a rate of 1%, decreased circumferential distortion by 60% at $M = 0.55$. Harrison et al. [14] experimentally and numerically investigated a suction and blowing scheme for a thick boundary layer ingesting a serpentine diffuser. At $M = 0.85$, they were able to reduce DC60 by 50% with a circumferential blowing scheme, but reduced DC60 by 75% by including suction. Garnier [15] performed spectral analysis comparing pulsed and continuous blowing in an aggressive s-duct using an array of dynamic pressure sensors and concluded that the pulsed blowing could match the performance of continuous jets at half the C_q over $M = 0.2 – 0.4$. Similarly, Salazar et al [16], found that pulsed jets were more effective than steady jets at reattaching separated flow inside a diffuser, and developed a retrospective cost adaptive control that allowed for real time optimization of jet frequency to further attach the flow and increase pressure recovery. Amitay et al. [17] used an array of synthetic jets to completely reattach flow in a serpentine duct up to $M = 0.2$, while Mathis et al. [18] also used synthetic jets to reattach flow through an S-duct diffuser at $Re = 4.1x10^4$. Gissen et al. [19] used a hybrid approach of passive vanes and synthetic jets in a boundary layer ingesting offset diffuser to improve circumferential distortion by 35% at $M = 0.55$. Burrows et al. [20] utilized fluidic-oscillating jets to control the vorticity of a modified offset diffuser and reduced distortion by 68% with $C_q = 0.0025$ at $M = 0.55$. In an extension study, Burrows et al. [21] were able to mitigate the effect of local flow separation in a serpentine diffuser and decreased circumferential distortion by 60% with $C_q = 0.005$. Finally, Burrows et al. [22] added a cowl to the same serpentine geometry that produced strong inlet streamwise vortices and significant total pressure losses. These were mitigated using aerodynamic bleed through the cowl.

These prior efforts clearly showed that AFC technology can be successfully used to mitigate the effects of adverse flow features within complex inlet designs. However, in earlier investigations, AFC has been incorporated into pre-existing fixed inlet designs as an *a posteriori* approach for improving performance. This inherently precludes investigating the interaction between flow control actuation and the geometric and operational space during the design stage. The overarching objective of the present work is to demonstrate the effectiveness of incorporating AFC early in the design process, enabling the use of shorter, more compact inlet diffusers. This was preceded by the development of a geometrically adaptive diffuser testbed that allows for rapid exploration of a range of compact-inlet geometric-design configurations as well as numerical simulation tools to allow for rapid variation of desired design characteristics [23]. The experimental testbed was designed and manufactured to allow rapid changes in the bend aspect ratio, cross sectional area, angle, and its radius of curvature, as well as changes to the diffuser shape, section lengths, and other parameters. In addition, the setup enables easy integration of AFC at multiple points throughout the diffuser to mitigate the adverse flow effects within the flow path.

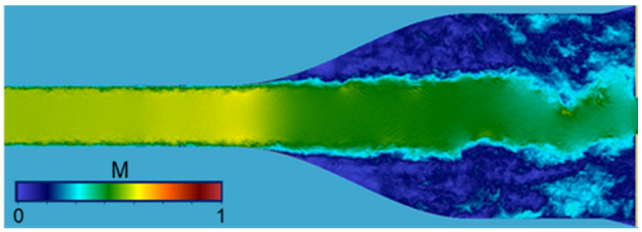

Figure 1. *A numerical illustration of fully separated flow entering an adapter from rectangular to circular cross-sectional area.*

The current effort expands on the earlier work of Fletcher et al. [24], who investigated a similar flow through a rectangular bend with a cross-section aspect ratio (AR) = 4. They found the main sources of the flow distortion and losses in the diffuser were associated with the onset of Dean circulations in the diffusers bend. As discussed by Fletcher et al. [24] and Li et al. [25], flow turning in the bend initiates streamwise vorticity concentrations along the side walls, and it was argued that Dean circulations advect these concentrations along the inner bend. Based on these findings, a flow control approach was devised to counter this vorticity transport over the upper surface using two mirrored spanwise arrays of yawed fluidically-oscillating jets along the same surface and/or along the sides. Fletcher et al. [24] demonstrated reduction of distortion by 60% and suggested successful counteraction of the advected vortices through the bend by the downstream flow actuation. Based on these findings, the present work expands on the earlier flow control approach by investigating a higher inlet aspect ratio and a smaller cross-sectional area. In the present flow geometry, the duct aspect ratio is increased to AR = 6, which transition to the round AIP imposes a steep pressure gradient across the upper and lower surfaces. Whereas the vortical structures associated with Dean circulation dominated alone the resulting flow total pressure losses and distortion in the prior work [24, 25], this work considers the coupling of such initiation of the streamwise vorticity with internal flow separation upstream from the AIP, as illustrated in Figure 1. Actuation is included on both the inner-bend and outer-bend surfaces to address both the adverse flow effects induced by the effect of unbalanced concentration of vorticity along the inner and outer halves of the bend. The test facility and diffuser design are presented in §II, the numerical setup and methodology are described in §III, and the underlying structure of the base flow is summarized in §IV. Finally, the proposed flow control approach is assessed in §V in the absence and §VI, in the presence of a bend.

II. Experimental Setup and Flow Diagnostics

The present experiments are performed in the Georgia Tech open-return, pull-down, subsonic wind tunnel driven by a 150 hp blower, as shown schematically in Figure 2, along with the diffuser model that replaces the test section. The programmable diffuser testbed is similar to the model that was used by Fletcher et al. [24], where it is described in more detail. Ambient air is drawn through a bellmouth with an inlet diameter $3.9D_{\mathrm{AIP}}$, followed by a circular to rectangular transition to the bend. An interchangeable bend section is connected to a short adapter that can house flow control modules and from there to a short diffuser and the AIP section. At the AIP, the time-averaged total pressure distribution is measured using a rake of 40 total pressure probes within a round conduit having a diameter D_{AIP} = 12.7 cm. Downstream of the total pressure rake section, the flow is expanded through the tunnel's diffuser and a 90-degree turn into the system's blower that is controlled by a variable frequency drive. The blower's outlet is connected to a flow silencer to reduce noise, and a water-cooled low-pressure drop heat exchanger (not shown) cooled by a chiller controls the return air to within 1-2° C.

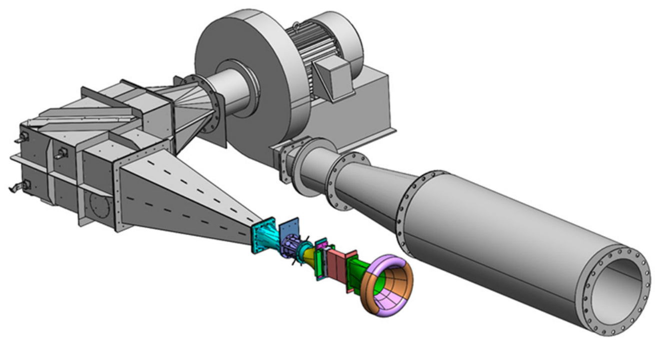

Figure 2. *CAD model of pull-down wind tunnel test facility having a straight modular diffuser model at the inlet.*

Two flow path configurations are shown schematically in Figure 3. Compared to the prior work [24, 25], where the transition adapter of the diffuser terminates in the AR = 4 rectangular section, an additional transition is added downstream from it, further increasing the aspect ratio to AR = 6. Its end can directly mate to the flow control adapter (Figure 3a) or to the bend (Figure 3b). In either configuration, the flow control adapter interfaces to the diffuser that smoothly transitions the AR = 6 rectangular geometry to the round AIP, as is also emphasized by the two contours in Figure 3. In principle, the design of the bend section allows for variations of the bend turning angle and turning radius [24] but the present investigation considered a straight flow path in the absence of a bend ($\theta = 0°$), focusing only on the flow separation, and that with the bend angle $\theta = 20°$ and radius $r/D = 0.35$, considering the coupling between the Dean circulation-induced vortices and flow separation; both over a range of bend Mach numbers $0.25 < M < 0.6$. It should be noted that while the model bends are configured horizontally, as shown in Figure 2, the experimental and numerical data are presented for vertical bending with the inner-bend surface at the top.

A 40-probe total-pressure rake at the AIP is assembled using eight radial arrays of five total pressure tubes positioned at $r/R = 0.27$, 0.38, 0.51, 0.67, and 0.9, that are spaced 45° apart azimuthally around the circumference of the AIP. The time-averaged total pressure measurements are used to compute the total pressure recovery as well as the flow distortion descriptors per SAE ARP1420C [26]. The total pressure rakes are supplemented with a matching array of eight static pressure ports that are each located on the diffuser wall, 0.4D upstream of the AIP. Another azimuthal array of eight equally spaced static pressure ports is located at the upstream end of the bellmouth and is used to compute the Mach number and mass flow rate through the diffuser using an earlier-developed calibration procedure [23]. The mass flow rate is normalized with respect to standard sea level pressure and temperature. Static and total pressures are measured using a PSI Netscanner system, where each set of pressure measurements is

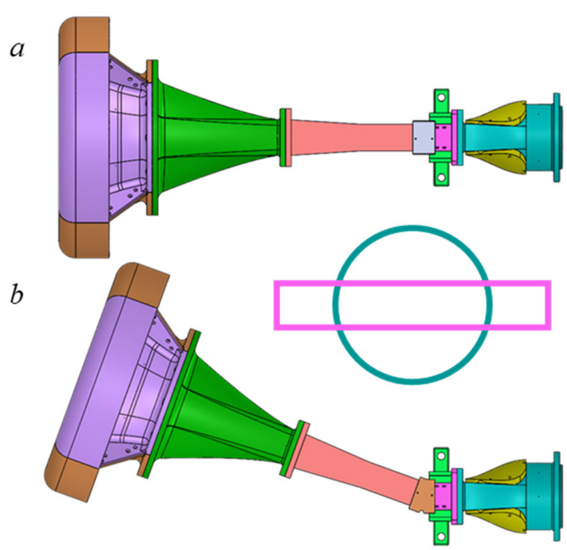

Figure 3. *CAD model of the modular diffuser at zero (a) and the bend angle of q = 20 ° (b). The bend's rectangular and the outlet (AIP) circular contours are also shown for reference.*

averaged over 64 independent samples, while the time-averaged static and total pressures are computed from fifty such sets. The manufacturer-specified accuracy is ±17.25 Pa, and the overall uncertainty of the time-averaged pressure is less than 1%. The static pressure around the circumference of the bellmouth is measured using a 10 torr *MKS Baratron* transducer (uncertainty of about 1.5 Pa) that is sampled using a computer-controlled rotary valve.

III. Numerical Setup

Flow Solver and Turbulence Model Large-eddy simulations (LES) were performed to simulate the flow through the experimental model examined in this study. The simulations were conducted using charLES [27], which solves the filtered compressible Navier–Stokes equations for mass, momentum, and total energy. The solver uses a density-based finite-volume formulation, with fluxes computed using a low-dissipation, entropy-preserving spatial discretization that is formally second-order accurate [27]. Time integration was performed using an explicit third-order Runge–Kutta scheme.

The simulations were performed on unstructured grids generated from Voronoi diagrams based on a hexagonally close-packed lattice of seed points [28]. This grid-generation approach produces smooth meshes composed of nearly isotropic polyhedral cells, which are well-suited for LES.

Near-wall effects were modeled using an algebraic equilibrium wall model. In this approach, the thin boundary-layer equations are assumed to be valid in the near-wall region, yielding a simplified momentum balance for a constant-stress layer in the wall-normal direction. The resulting equation is solved algebraically at each wall-adjacent cell centroid and at each time step to determine the wall shear stress, which is then imposed as a Neumann boundary condition for the momentum equations [29]. The model does not explicitly account for inner-layer unsteadiness or pressure-gradient effects, but it substantially reduces the near-wall grid resolution required for LES. This approach is therefore referred to as wall-modeled LES (WMLES). Subgrid-scale stresses were modeled using the dynamic Smagorinsky model [30].

Computational Domain and Simulation Details The computational domain used for the diffuser simulations is shown in Fig. 4 and was generated from the CAD model of the experimental facility and test-section hardware. The AFC module was installed downstream of the bend, as shown in purple. For the baseline case, the AFC module was removed and replaced with a flat wall. The bellmouth was extended upstream, as shown in yellow, to include a large hemispherical inlet region. This extension ensured that the far-field velocities remained small relative to the internal flow. A total-pressure boundary condition was applied at the hemispherical inflow surface using standard-day atmospheric conditions. The tunnel walls were modeled as no-slip walls with the algebraic equilibrium wall model applied. The numerical extensions downstream of the AIP were modeled as free-slip walls. At the outlet, a static-pressure boundary condition was imposed, with the

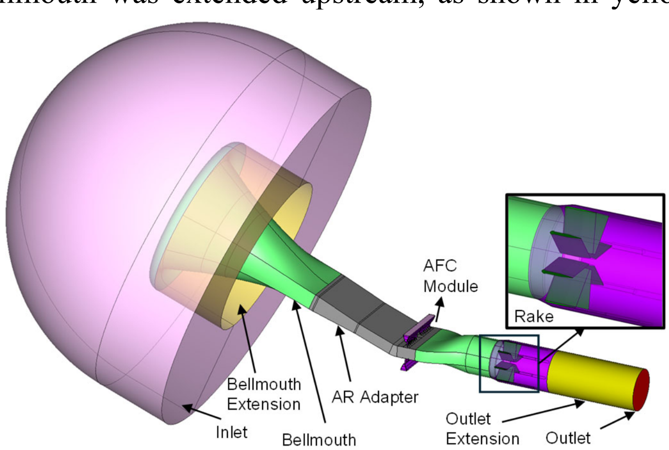

Figure 4. *Numerical model of the q = 20° bend test configuration.*

pressure adjusted to achieve the desired mass flow rate at the AIP. For the AFC cases, a mass-flow boundary condition was applied at the AFC plenum inlet to impose the target mass-flux coefficient C_q. The AFC array contained jets along both the bottom wall and the top wall. These two jet groups were supplied by separate inflow boundaries, allowing the top and bottom jets to be activated independently. The summary of cases studied is shown in Table 1.

Table 1. WMLES Summary of Cases

Case	θ(°)	*r/D*	*Cq*		M_{AIP}
			Top	Bottom	
1	0	N/A	0	0	0.34
2	0	N/A	0.0925	0.0925	0.34
3	20	0.2	0	0	0.34
4	20	0.2	0.0105	0.0065	0.34

The grids used in this study were based on prior mesh-development work for the AFC testbed configuration and the baseline tunnel grid-sensitivity study. Details of the mesh-generation procedure and validation are provided by Stratton et al. [23]. The baseline and AFC simulations used approximately 390 million control volumes. The average wall-normal resolution, measured using y^+along the no-slip walls shown in gray in Fig. 4, was less than 31 for all configurations.

All simulations were run on the U.S. Department of Defense Blueback and Wheat high-performance computing clusters using GPU resources. On 40 NVIDIA A100 GPUs, the solver advanced approximately 40 characteristic diffuser flow-through times in 24 hours, where the characteristic time scale was based on the convection time between the throat and the AIP.

IV. Base Flow Characteristics

More details on the base flow in similar geometries were presented by Fletcher et al. [24] and Li et al. [25], and further assessment of such flow features will also be presented in direct comparisons with the controlled flows in §V and §VI. Variations of three flow descriptors at the AIP with respect to the change in Mach number upstream from the bend/flow control module are shown in Figure 5 for the base flow case. Recovery, defined as the 40-probe averaged total pressure across the AIP face relative to ambient pressure, is utilized as a measure of the total pressure losses. Many distortion descriptors exist to define the spatial distributions of total pressure deficit at the AIP and

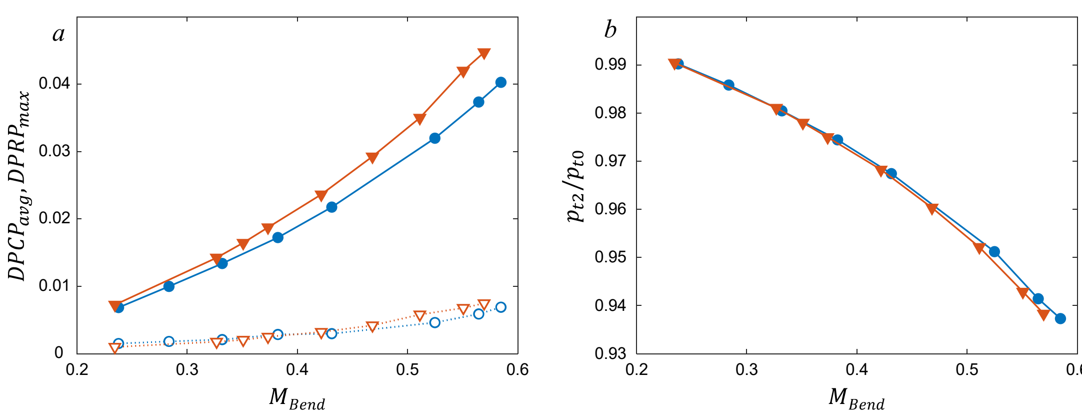

Figure 5. *Variation of the distortion parameter $DPCP_{avg}$ and $DPRP_{max}$ (a) and pressure recovery p_{t2}/p_{t0} (b) with bend Mach number for θ = 20° and r/D = 0.35 (▼ $DPCP_{avg}$, ▽ $DPRP_{max}$) and θ = 0° (● $DPCP_{avg}$, ○ $DPRP_{max}$).*

are primarily engine dependent. Still, a typical circumferential distortion parameter $DPCP_{avg}$ [26], is considered as the primary distortion descriptor in this work. In addition, redistributions of the deficit patterns at the AIP that result in improvements in circumferential distortion often may have detrimental effect on the radial distortion. Hence, an additional distortion parameter, $DPRP_{max}$ [26], is considered, which is defined by the maximum normalized deviation of the ring-averaged total pressure to the face-average total pressure over the five 8-probe rake rings. It is noted that the maximum, rather than the average $DPRP$ is used since the $DPRP_{avg}$ is zero by definition.

Baseline flow distortion descriptors are shown in Figure 5a in the absence ($\theta = 0°$) and presence of a bend ($\theta = 20°$) in the flow path. Circumferential distortion parameter $DPCP_{avg}$ exhibits a typical nonlinear increase with Mach number, exceeding $DPCP_{avg} = 0.04$ at the highest Mach number tested. Also, as expected, coupling a bend upstream of the separated flow further increases distortion since the $DPCP_{avg}$ curve for the bend is fully displaced upward relative to the straight flow path. Relative to circumferential distortion, the magnitudes of the maximum radial distortions are significantly smaller, not exceeding $DPRP_{max} = 0.01$ even for the highest Mach numbers. Although the flow path without the bend also results in smaller maximum radial distortions, these differences are nearly negligible. The total pressure recovery, seen in Figure 5b, also exhibits a typical nonlinear decrease with Mach number. Moreover, differences between the two flow paths are less pronounced, with the flow through the bend incurring slightly higher losses. It should be noted that, even without any prior knowledge of the actual flow fields, the levels of total pressure losses, up to about 6%, indicate non-smooth traversing of the flow through the tested geometries. Total pressure distortions can attain rather high values even in the absence of flow separation, due to the strong secondary flows as shown by Fletcher et al. [24], while the excessive drop in recovery is closely associated with a presence of flow separation and possibly transonic shocks in the flow.

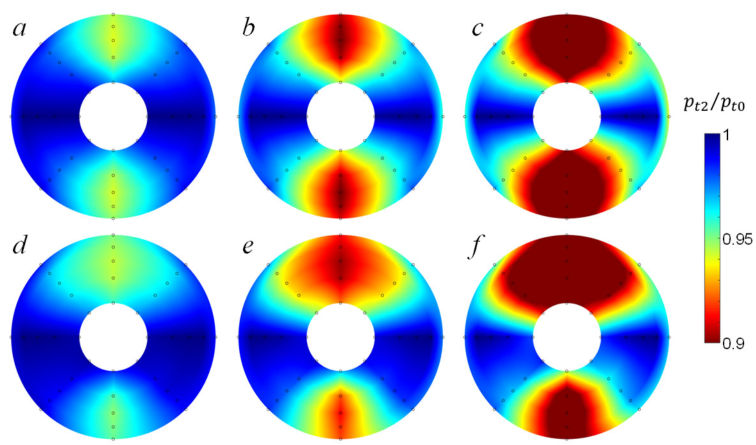

Figure 6. *Color raster plots of the total pressure distribution measured at the AIP for no bend (a,b,c), and θ = 20°, r/D = 0.35 bend (d,e,f), for* $M_{AIP} = 0.22$ *(a,d),* $M_{AIP} = 0.29$ *(b,e), and* $M_{AIP} = 0.34$ *(c,f).*

To illustrate the base flow total pressure distributions at the AIP associated with the flow descriptors, Figure 6 shows color raster plots of the measured total pressures by the 40-probe rake over three Mach numbers. For the straight flow path (Figure 6a – c), the total pressure deficit is symmetric about the horizontal axis and centered about the diffusing sides of the adapter/diffuser upstream of the AIP, due to the symmetric sources of the deficit – symmetric flow separation on both surfaces. As the Mach number increases, these deficit domains grow both in spatial extent and in magnitude, resulting in the highest distortion coefficient $DPCP_{avg} \approx 0.04$ and the lowest recovery 0.936 (Figure 6c). Once the bend is included in the geometry, two different features are noted in the deficit domains. Aligned with the inner bend (top), there is an amplification of the total pressure deficit region due to the inner bend-induced streamwise vorticity coupling to the downstream flow separation along the inner-bend surface of the diffuser. Moreover, it appears that amplification of the total pressure losses on that side couples to a lesser deficit on the opposite side (bottom) that is aligned with the outer bend surface. Since the total pressure deficit becomes even more nonuniform across the AIP in the flows with the bend (Figures 6d – f), it is expected that the circumferential distortion is increased relative to the no-bend case, reaching the highest $DPCP_{avg} \approx 0.045$ (Figure 6f).

V. Flow Control of a Straight Flow Path

The present flow separation over diffusing sides bears similarities with the prior case of flow separation in a serpentine diffuser past its second turn [21]. This similarity suggests that prior successful flow control approaches could be adopted for the current problem with a distributed array of flow control elements just upstream of the incipient separation. However, instead of likely just adopting such an already-known flow control approach, it is chosen to test the feasibility of the flow control array developed for flow control of secondary flows [24] in absence of flow separation, where the flow control array was displaced upstream from the diffuser. This approach is motivated by the possibility of using a single flow control unit regardless of whether there are separation domains in the flow, which, in the presence of a bend, couple to the upstream secondary flows.

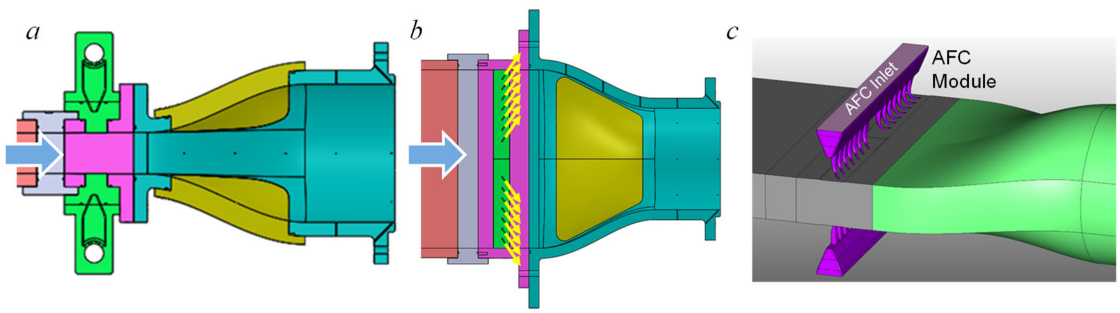

Figure 7. *Cross-sectional side (a) and bottom (b) views of the two experimental flow control modules integrated upstream from the diffuser adapter, and the corresponding numerical model (c).*

Experimental and numerical incorporations of active flow control are shown in Figure 7. Figure 7a illustrates integration of the two flow control modules (in green) upstream of the diffuser, where the upper module mimics that used by Fletcher et al. [24]. This module is mirrored onto the opposite end as well, since the flow separates on both sides of the diffuser in the present geometry. Each flow control module is comprised of an outer plenum module driven by compressed air and a jet array module that is driven uniformly by the plenum. The actuation modules can be easily installed or removed from the diffuser, and the jet modules can also be reconfigured by disabling individual jets. Figure 7b illustrates the top jet array, where each jet is represented by arrows. It consists of 14 yawed rectangular surface jets (7 on each side) having orifices that are 1.3 mm wide and 1.7 mm in height. The jets are yawed at 55° relative to the streamwise direction to induce streamwise vorticity concentrations of opposing sense to the streamwise vorticity in the base flow. Numerical incorporation of the control jets includes only the plenum volume and the jets' paths (Figure 7c), where the targeted mass flow rate is imposed as the boundary condition at the plenum. Separate inflow boundaries are defined for the two flow control modules, allowing the top and bottom jet arrays to be activated independently.

The fluidic control module was bench tested and characterized, and the three components of its thrust were measured and calibrated over a range of actuation mass flow rate $\dot{m}_j$ to obtain $|\vec{T}| = f(\dot{m}_j)$. These data were used to compute the actuation mass flow rate coefficient $C_q = \dot{m}_j/\dot{m}$ and the (thrust-based) momentum coefficient $C_\mu^F = |\vec{T}|/|\vec{P}|$, where $\dot{m}$ and $\vec{P}$ are the diffuser's mass flow rate and momentum rate, and $\dot{m}_J$ and $\vec{T}$ are the jet's mass flow rate and thrust, following the procedure outlined by Fletcher et al. [24].

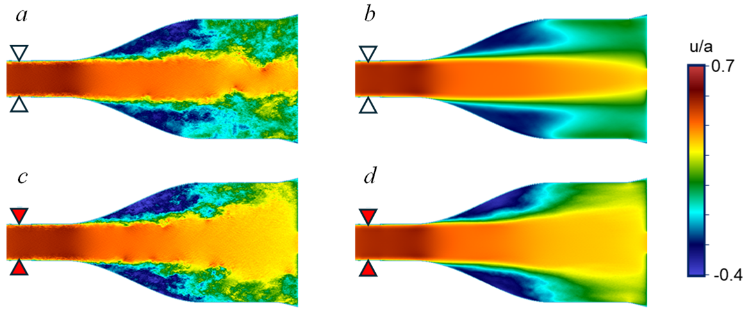

Figure 8. *Cross-sectional views of instantaneous (a,c) and time-averaged (b,d) streamwise velocity for the baseline (a,b) and the flow controlled by both jet arrays (each C_q = 0.0092) over a straight path (θ = 0°), for the upstream M ≈ 0.49.*

An initial illustration of the flow control effect is shown by numerical results depicting the streamwise velocity component of flows into the diffuser and to the AIP, as seen in Figure 8. Both the base/uncontrolled flow and the flow controlled by both flow control modules, at C_q = 0.0092 each, are shown. To illustrate the corresponding snap shots of the flow, instantaneous flow fields are shown in Figures 8a and c. The controlled flow that separates upon entrance into the diffuser does not seem to change from the base flow, but the differences become prominent downstream from the initial flow separation. Since the flow entering the diffuser through the AR = 6 duct cannot navigate steep diffusing sides, the initial flow structure resembles a rectangular jet issuing into confined space in both the controlled and uncontrolled flows. However, the effect of the flow control arrays is clearly manifested through the "jet" enhanced spreading toward the surface as the flow evolves into the AIP. This effect is even more amplified in the time-averaged flow fields shown in Figures 8b and d. As expected, the extent of the separation bubble remains practically unchanged in the control flow because the upstream actuation mechanism was originally designed to target the main vorticity sources in the absence of flow separation [24]. Nonetheless, some of the compression of the radial extent of the separated domain is seen in the controlled flow as a secondary effect of the "jet" spreading. The main effect of the active flow control is seen in the jet amplified radial spreading into the AIP, which ultimately results in much lower velocity deficit, which is also reflected in the total pressure as well, in the annular region close to the surface.

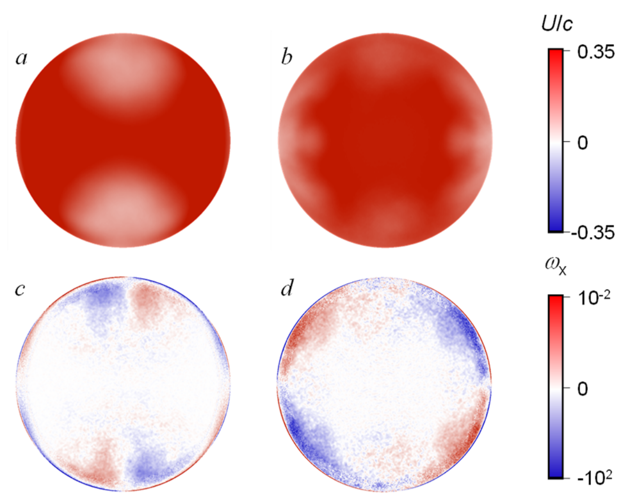

Figure 9. *Color raster plots of the streamwise velocity (a,b) and vorticity (c,d) for the baseline (a,c) and the flow controlled by both jet arrays (each C_q = 0.0092) over a straight path (θ = 0°), for the upstream M ≈ 0.49.*

Figure 9 illustrates the flow state at the AIP for the base and controlled flows discussed in Figure 8. Time-averaged streamwise velocity component of the base flow (Figure 8a) indicates two large velocity deficit domains that are clearly associated with the total pressure deficit domains already seen in Figure 6 as streamwise velocity contributes to those total pressure distributions. These deficit domains are also indicative of three-dimensionality of the upstream flow separation that precedes the velocity deficits at the AIP. As a result of flow control, the AIP distribution of the streamwise velocity component becomes significantly altered (Figure 9b) despite prior indications that the control does not significantly alter the separation bubble itself (cf. Figure 8). In the core flow at the AIP, there is much better organization of the like-momentum flow. There are still some, albeit weak, remnants of the velocity deficits of the base flow and it appears as if most of the deficit in the base flow becomes redistributed azimuthally, thus forming the outer ring of mild deficit in addition to the improved core flow. To understand better the flow features that are associated with these changes, the mean streamwise vorticity is also shown in Figures 9c and d, corresponding to the shown velocity plots. In addition to the near-wall vorticity layers, the mean base flow (Figure 9c), is comprised of two pairs of counter-rotating vortex pairs, each centered about the upstream flow separation. In previous works, such vortex pairs were formed about the inner bend even in the absence of flow separation and were caused by the accumulation of the wall-layer vorticity due to Dean circulation [24]. In the present flow, it is expected that incipient Dean circulation becomes disrupted due to the massive local flow separation. However, the vortical composition of the flow on the upper side of the AIP remains strikingly similar to the prior flows without separation [24]. In addition, the same vortical composition was characteristic for the flow within a serpentine diffuser [21] along the side of a local flow separation, past the second bend. The controlled flow (Figure 9d) exhibits four vortical structures, distributed by quadrants and elongated along the surface. It should be noted that these vortices are not simply azimuthally displaced vortices of the base flow since they possess altered senses of rotation.

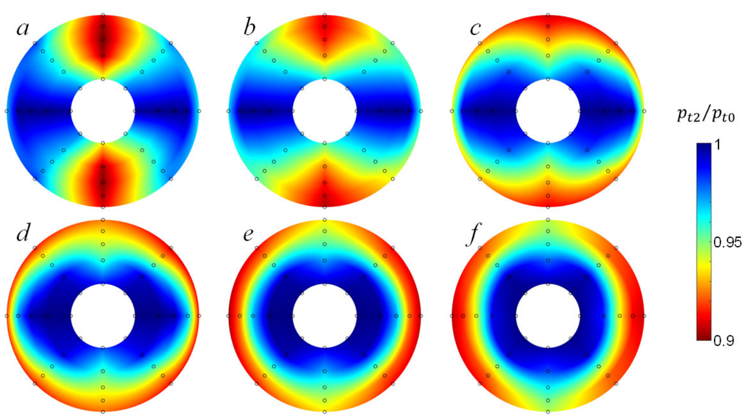

Figure 10. *Color raster plots of the total pressure distribution measured at the AIP for the dual jet-array control over a straight flow path configuration (θ = 0°) at M_{AIP} = 0.29 and the total C_q = 0 (a), C_q = 0.0066 (b), C_q = 0.0098 (c), C_q = 0.0121 (d), C_q = 0.0164 (e), and C_q = 0.0197 (f).*

Gradual change in the total pressure distribution at the AIP with increasing the flow rate coefficient C_q, applied equally between both flow control modules, is shown in Figure 10 for M_{AIP} = 0.29 flow. Several key features of the progressive redistribution of the total pressure deficit are noted. An initial retreat of both deficit domains is associated with radial retraction towards the surface and azimuthal spreading (Figure 10b). The near-surface azimuthal spreading progresses rapidly for the next increase in C_q (Figure 10c), reaching the nearly uniform azimuthal deficit distribution over a thin wall region in the next step (Figure 10d). However, while facilitating such a uniform redistribution near the surface, the core distribution forms an elliptical shape with the major axis horizontal. By further increasing C_q, the central top and bottom near-wall zones improve even further in the deficit reduction at the expense of some thickening of the rest of the azimuthal layer. However, the core region becomes fairly axisymmetric, as seen in Figure 10e. Finally, if C_q is even further increased, the top and bottom local zones continue to reduce the total pressure deficit, with further thickening of the azimuthal ring near the surface (Figure 10f). In addition, the previously axisymmetric core begins to stretch into an elliptical form but with the major axis vertical. Overall, different total pressure patterns with flow control can be tailored by varying C_q. It is also important to note that, from the standpoint of circumferential distortion, it is likely the most desirable to induce as axisymmetric total pressure distribution as possible, which can clearly be attained between the major axis switch from horizontal to vertical. Among the cases shown in Figure 10, the most axisymmetric pattern is shown in Figure 10e. Indeed, when comparing $DPCP_{\text{avg}}$ descriptors for the shown cases, the lowest controlled case is associated with that distribution, yielding $DPCP_{\text{avg}}$ = 0.0065, down from $DPCP_{\text{avg}}$ = 0.0265 for the baseline case (Figure 10a).

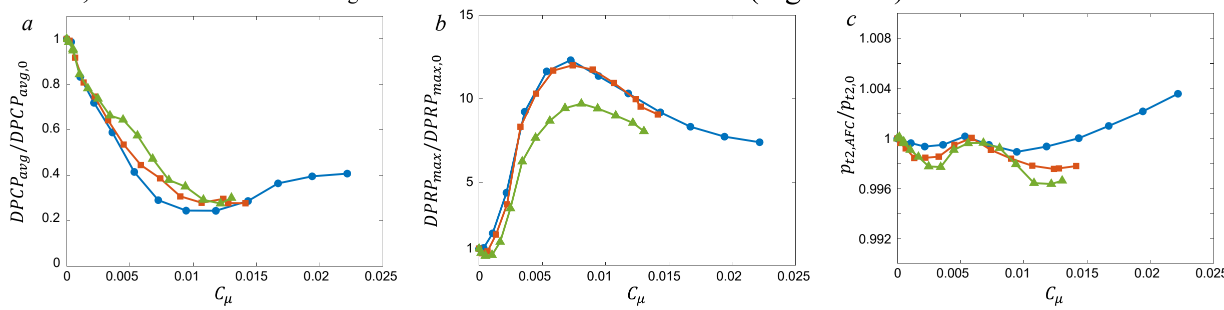

Figure 11. *Variation of the distortion parameter $DPCP_{avg}$ (a, b), $DPRP_{max}$ (c, d), and pressure recovery p_{t2}/p_{t0} (e, f) with the jets' mass flow rate (a, c, e) and momentum (b, d, f) coefficients for M_{AIP} = 0.22 (●), 0.29 (■), and 0.34 (▼).*

A summary of the controlled flows for the straight flow path (θ = 0°) is shown in Figure 11, in terms of the average circumferential distortion $DPCP_{\text{avg}}$, maximum radial distortion $DPCP_{\text{max}}$ and recovery. Each of these descriptors is plotted relative to the baseline flow (C_{q} = 0) and with respect to the jets; momentum coefficient C_μ, as it was shown by Fletcher et al. [24] that a closer collapse of data points is achieved relative to the mass flow rate coefficient C_{q}. Although with some deviation, the $DPCP_{\text{avg}}$ distributions across the three Mach numbers (Figure 11a) indicate similar sharp response of the flow with C_μ, reaching the minimum at about 70% reduction for $C_\mu \approx 0.05$. Once the plateau is reached, further increase in C_μ causes a detrimental effect that is clearly seen for the lowest Mach number (as also seen in prior studies). Hence, a true optimum in $DPCP_{\text{avg}}$ can be sought. Even before estimating radial distortion, it can be expected that the controlled total pressure patterns at the AIP, being radially "stratified" (cf. Figure 10) would adversely affect the radial distortion. Indeed, Figure 11b indicates a sharp rise in the maximum radial distortion, as a tradeoff for the dramatic drop in the circumferential distortion. The relative rise in the peak radial distortion is also amplified due to the very low baseline levels (cf. Figure 5a). While the distributions seen in Figure 11b show a nearly perfect data collapse for the two lower Mach numbers, data for the highest Mach number deviates from such unified responses, possibly indicating some change in the underlying physics. Another interesting observation related to $DPRP_{\text{max}}$ is that, after initial steep rise, it reaches its peak, although not at the same $C_\mu \approx 0.06$ for which $DPCP_{\text{avg}}$ attains its minimum. Finally, recovery in general does not change, indicating a fraction of a percent decrease in most scenarios, as seen in Figure 11c.

VI. Flow Control in the Presence of a Bend

As indicated in the base flow analysis in §IV, the introduction of a bend (θ = 20°, r/D = 0.35) induces the total pressure top-to-bottom asymmetry, where the deficit aligned with the inner bend increases relative to the no bend, while the deficit aligned with the outer bend side decreases. Consequently, there is some uptick in the circumferential distortion, paired with a very small drop in recovery. Different distortion domains at the top and bottom of the AIP have an important ramification for the flow control application, as it also forces asymmetric flow control coefficients to be applied to each domain.

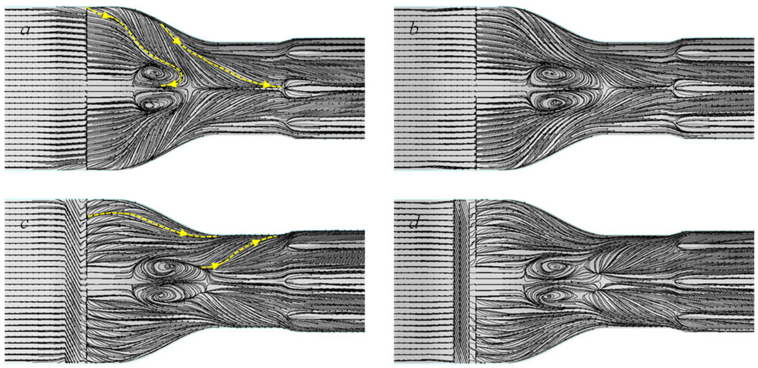

Figure 12. *Near-surface flow topology along the top (a,c) and bottom (b,d) surface downstream from the* θ *= 20° bend geometry and the upstream M* $\approx$ *0.49, for the baseline (a,b) and the flow controlled by the top (*C_q *= 0.0105) and bottom (*C_q *= 0.0065) jet arrays.*

One illustration of the resulting near-surface streamlines projected onto the surfaces is shown in Figure 12 for the local flow control coefficient C_q = 0.0105 at the top (inner bend) and 0.0065 at the bottom (outer bend), for Mach number at the bend of $M \approx 0.49$. In general, only secondary differences are seen for the flow evolutions over the inner (top) and outer (bottom) surfaces, where the main flow topologies of the base and controlled flows remain similar. Therefore, the main differences between the base and controlled flow topologies are emphasized only on the top surface in Figures 12a and c. In the base flow (Figure 12a), a central separation bubble forms, with the upstream flow focused toward the bubble, emphasized by the upstream streamline in yellow. Past the stagnation point immediately downstream from the bubble, the flow from the sides continues to focus toward the central dividing line feeding into the vortex pair thereby forming at the tail end of the separation bubble and enhancing the vortices as they evolve into the AIP. This second characteristic, near-surface flow is also marked by the second highlighted streamline in yellow. Once the flow control is applied (Figure 12c), this near-surface flow topology becomes vastly altered. Due to the jets' yawed orientation toward the sides, the upper topology upstream of the separation bubble becomes initially swept to the side, forming small-scale vortices that do not feed into the bubble, as emphasized by the highlighted streamline in yellow. The second major change is seen in the streamlines of the separation bubble envelope. Although the separation bubble imprint at the surface becomes somewhat enlarged (but shallower, cf. Figure 8), the flow off its envelope diverges to the sides, rather than converging into the vortex pair about the central plane. By losing that source of the surface vorticity, this vortex pair forms into a much weaker structure than in the case of uncontrolled flow. Overall, the flow topologies shown in Figure 12 indicate a completely altered baseline flow topology under the upstream flow control.

To further elucidate the mechanisms by which flow control generates such dramatic changes in the flow topology that were assessed in Figure 12, the streamwise evolution of the flow is traced across several cross sections, down to the AIP ($x = 0$) in Figure 13. Each plane is represented by a composite image, where half the plane shows raster plots of the time-averaged streamwise vorticity component, and the other half emphasizes a full cross-stream flow topology by plotting in-plane pseudo streamlines. It is noted that such pseudo streamlines do not carry any information about the magnitudes of those motions, only the structure. As discussed in previous work [24], in the absence of flow control, the bend-induced Dean circulations advect vorticity along the sidewalls as seen in the most upstream flow in Figure 13a-1. As the base flow progresses downstream (Figure 13b-1), the vorticity layer along the side walls gets transported up and along the upper surface / inner bend, where its accumulation becomes disrupted by the central flow separation, as seen at the next plane (Figure 13c-1). However, such a separation-delayed central accumulation of vorticity continues about the separation domain, finally merging into a vortex pair downstream from the separation bubble (Figure 13d-1), and the flow topology at the AIP becomes clearly distinguished by the pair

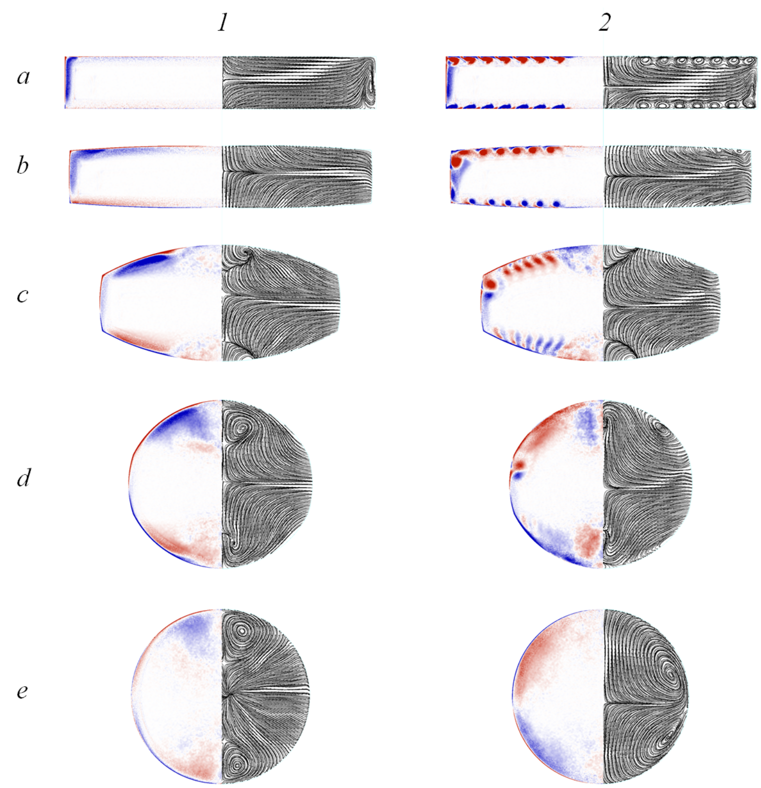

Figure 13. *Composite cross-sectional half-planes of time averaged vorticity and in-plane pseudo streamlines for the θ = 20° bend geometry and the upstream $M \approx 0.49$, for the baseline (1) and the flow controlled by the top (C_q = 0.0105) and bottom (C_q = 0.0065) jet arrays (2) at x/D = -2 (a), -1.6 (b), -1 (c), -0.8 (d), and 0 (e).*

of counter-rotating vortices in the upper region, much like in the case of the flow in the absence of separation [24]. The presence of flow separation domain on the outer bend side (bottom) is seen to also induce accumulation of the vorticity layer that proceeds to roll into the second, albeit weaker vortex pair along the bottom side of the AIP. Whereas an equivalent roll up in the absence of separation [24] resulted in a very weak vortex pair, primarily attributed to Görtler vortices [31], the large-scale vortex pair formation becomes significantly enhanced in the presence of flow separation. This is arguably due to the flow acceleration and curving around the separation bubble, transforming some of the spanwise-oriented vorticity into streamwise component (Figure 13c-1), followed by transporting the surface vorticity layer towards the central plane downstream from the separation bubble (Figures 13d-1 and 13e-1). Once the flow control is applied, a typical array of small-scale vortices is formed, seven on each half plane (Figure 13a-2). These vortices, by design, oppose and destructively interact with the opposite-sense surface vorticity layers. By the next plane (Figure 13b-2), the next to the outer jet vortex becomes engulfed by the most outer vortex (the joint vortex is seen at the next plane), while the remaining five jet vortices approach each other and begin to coalesce in the same plane (Figure 13c-2). It is also noted that around the separation bubble, there is still a weak accumulation of the CW vorticity, arguably due to the transport of surface vorticity of the diverted flow around the separation bubble, similar to the mechanism on the opposite side, as seen in the same plane. By the next plane (Figure 13d-2), five jets coalesced into a single elongated vortical structure, which appears to engulf small scale same-sense vortices on their sides by the AIP plane (Figure 13e-2). Interestingly, the weaker vortex pairs at the top and bottom, the remnants of the baseline vortices, seemingly diffuse by the AIP plane, leaving only four-quadrant vortices, which all originated from the control jets.

To illustrate the effects of isolated flow control applied to only one side of the bend, inner or outer, Figure 14 shows the resulting total pressure raster plots measured at three Mach number flows, when the control is applied by the jets' fixed control rate, which, due to the difference in Mach numbers results in decreasing C_qs with increasing M. The base flows are shown in Figures 14a – c for reference. When the flow control over the inner bend side (top) is applied at the lowest Mach number at C_q = 0.0164, it fully recovers total pressure in that region (Figure 14d), arguably due to the successful mitigation of flow separation. A somewhat weaker but still robust effect on recovery of

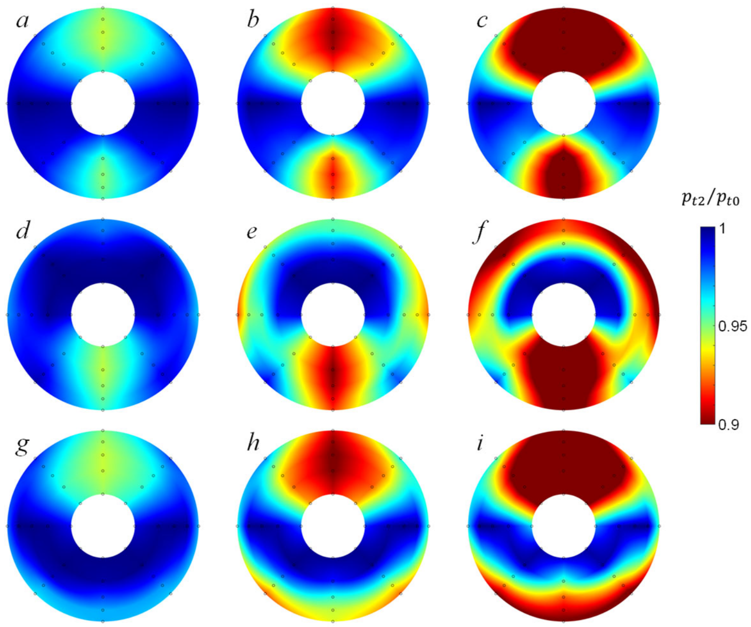

Figure 14. *Color Raster plots of the total pressure at the AIP of the θ = 20°, r/D = 0.35 bend at M_{AIP} = 0.22 (a,d,g), 0.29 (b,e,h), and 0.34 (c,f,i), for base flow (a,b,c), flow control applied along the inner bend (d,e,f) at C_q = 0.0164 (d), C_q = 0.0131 (e), and C_q = 0.0115 (f), and flow control applied along the outer bend (g,h,i) at C_q = 0.0084 (g), C_q = 0.0066 (h), and C_q = 0.0058 (i).*

the core flow deficit is seen for the middle Mach number (C_q = 0.0131) in Figure 14e. While a similar effect is seen for the core flow at the highest Mach number (Figure 14f) with a further decrease in C_q and an increase in the azimuthal near-surface deficit. Not surprisingly, similar effects are attained by activating only the jet array on the opposite (bottom) side; however, the generally lower C_qs that were utilized induced a lower azimuthal spread of the residual deficit. In principle, both sets of controlled jets demonstrated robust effects along surfaces of their domains when operated individually.

Since different levels of total pressure deficit in the baseline flow are associated with the inner and outer bend sides, asymmetric control authority over the top and bottom surfaces is clearly required. A subset of indicative effects on the distortion descriptors for different C_qs applied to the inner and outer bend surfaces is shown in Figure 15 for the same three Mach number flows illustrated in Figure 14. All the descriptors are shown relative to the base flow values, and their variations are plotted with respect to the C_q of the inner jet array and three variations of the outer jet array, no control ($C_{q,outer}$ = 0) and two levels of control $C_{q,outer1}$ and $C_{q,outer2}$. Interestingly, when applying flow control only over the inner bend side ($C_{q,outer}$ = 0), very little improvement in the $DPCP_{avg}$ can be attained regardless of the magnitude of the $C_{q,inner}$ and of the Mach number flow (Figures 15 a – c). This is attributed to the deficit only improving on one half of the AIP plane, which in turn has also a negative impact on the axisymmetry across the full AIP plane. Adding a small level of outer bend control to the inner bend results in an initial drop in $DPCP_{avg}$ with $C_{q,inner}$, up to 50% for the lowest Mach number (Figure 15a) before increasing for the higher $C_{q,inner}$. When $C_{q,outer}$ is increased, a considerably deeper drop in $DPCP_{avg}$ with $C_{q,inner}$ is attained, reaching nearly 60% even for the highest Mach number (Figure 15c). The corresponding increase in $DPRP_{max}$, as already discussed with respect to Figure 11, seems to be proportional to $C_{q,outer}$ and inversely proportional to Mach number, as seen in Figure 15d – f. Contrastly to $DPCP_{avg}$, this parameter has a local peak with increasing $C_{q,inner}$, regardless of the level of $C_{q,outer}$. Finally, as already seen in other examples, the effect of the flow control on recovery is small in any of the cases considered in Figures 15g – i, as it appears marginally beneficial or neutral for the three Mach numbers considered.

Changes in the flow structure at the AIP, with and without the flow control, are emphasized in Figure 16, where the time-averaged axial, radial, and azimuthal velocity components are plotted as raster plots, in addition to the flow angularity. As already seen for the geometry without the bend (Figure 9), streamwise velocity deficits associated with large-scale vortical structures of the base flow

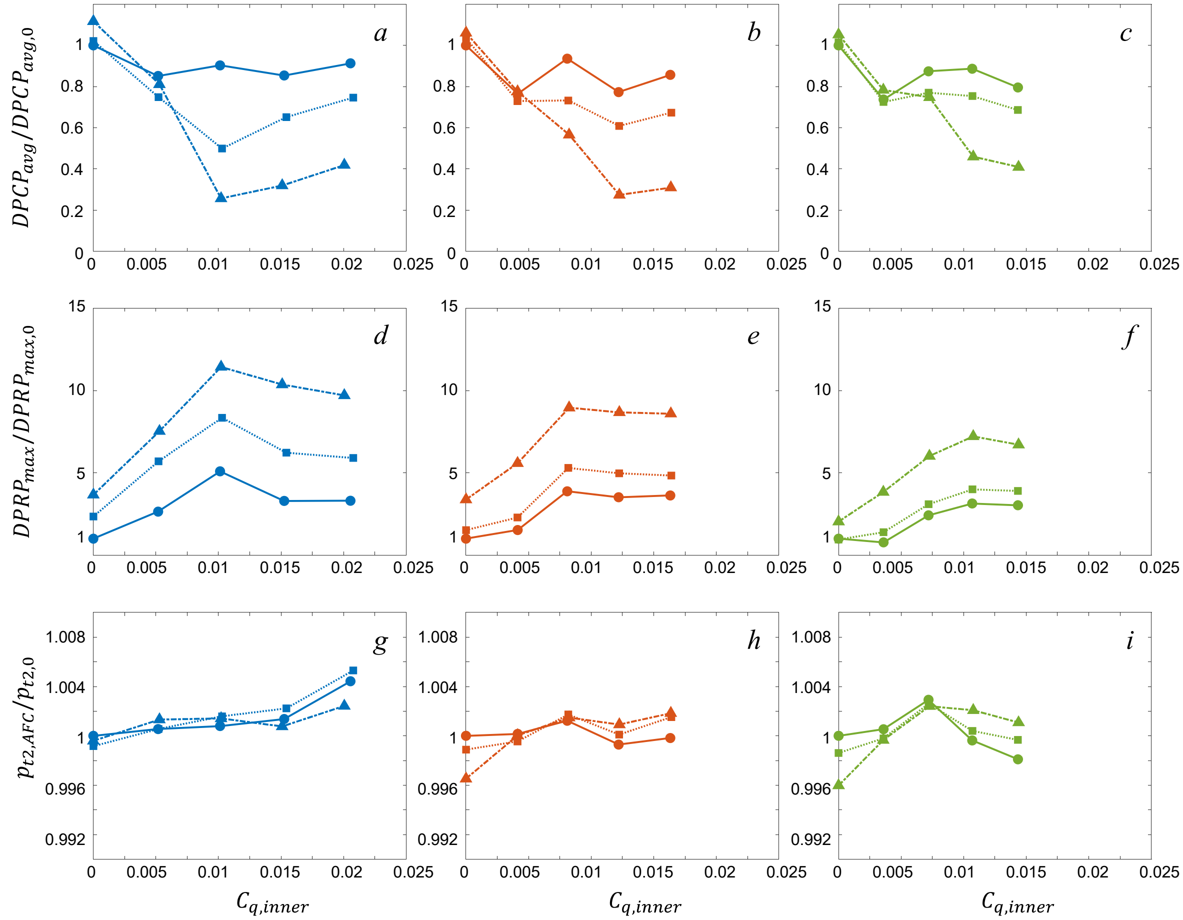

Figure 15. *Variation of the distortion parameter $DPCP_{avg}$ (a, b, c), $DPRP_{max}$ (d, e, f), and pressure recovery p_{t2}/p_{t0} (g, h, i) for M_{AIP}=0.23 (a, d, g) and $C_{q,outer}$= 0 (●-), $C_{q,outer}$= 0.0041 (■ •••), and $C_{q,outer}$= 0.0082 (▼- -) (a, d, g) , M_{AIP}=0.29 (b, e, h) and $C_{q,outer}$= 0 (●-), $C_{q,outer}$= 0.0033 (■ •••), and $C_{q,outer}$= 0.0065 (▼- -) (b, e, h) , and M_{AIP}=0.34 (c, f, i) and $C_{q,outer}$= 0 (●-), $C_{q,outer}$= 0.0029 (■ •••), and $C_{q,outer}$= 0.0058 (▼- -) (c, f, i).*

(Figure 16a) become significantly suppressed in the controlled flow (Figure 16e) at the expense of redistributed deficit azimuthally but enabling a more uniform core flow at the AIP. Regardless of whether the flow is controlled or uncontrolled, both radial and azimuthal velocity components remain much smaller than their respective streamwise components, but there is a clear restructuring of the flow under the flow control. In the base flow, radial flow is predominantly outward relative to the bulk flow, except for the inward pockets associated with vortex pairs at the top and bottom (Figure 16b), while such domains grow completely to the core with the 90° pattern shift in the controlled flow (Figure 16f). Similarly, the azimuthal velocity components in the baseline flow (Figure 16c) are clearly associated with the two vortex pairs and become spread across the whole AIP (Figure 16g), along with the vortical flow composition of the controlled flow. Clearly, observed changes in the two in-plane velocity components affect the resulting flow angularity at AIP. The base flow angularity reaches the highest levels about the two vortex pairs (Figure 16d), while the controlled flow balances angularity better across the core flow, at the expense of high angularity in four quadrants near the surface (Figure 16h), which is also associated with the azimuthal shifts of the four large-scale vortical structures in the controlled flow fields.

More insight into the flow composition at the AIP and its changes with flow control is sought through

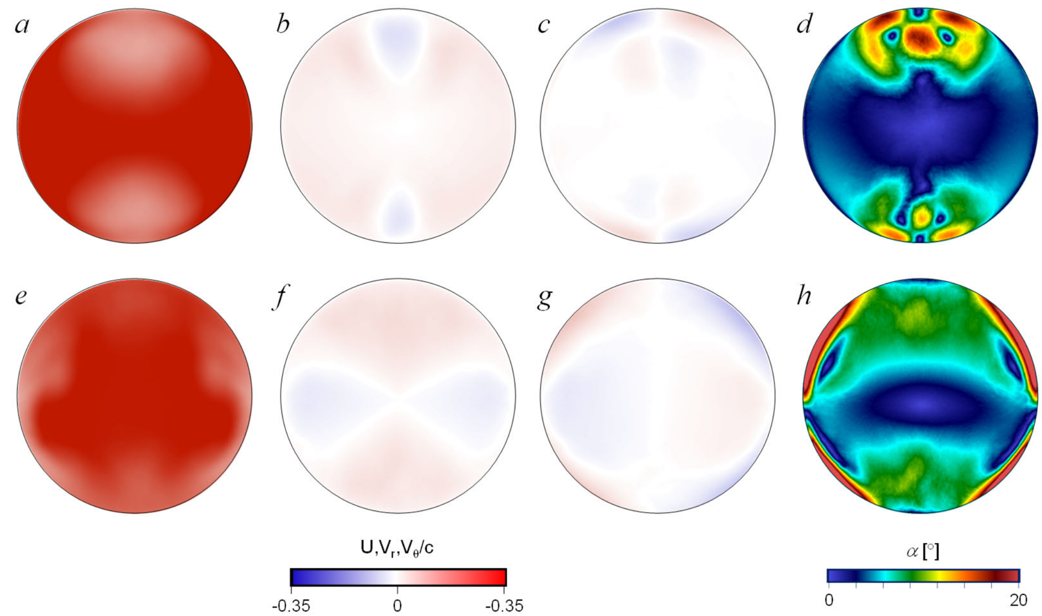

Figure 16. *Color raster plots of the time-averaged streamwise (a,e), radial (b,f), and azimuthal (c,g) velocities, and the flow angularity (d,h) at the AIP for the $\theta = 20°$ bend geometry and the upstream $M \approx 0.49$, for the baseline (a–d) and the flow controlled by the top (C_q = 0.0105) and bottom (C_q = 0.0065) jet arrays (e–h).*

vorticity and turbulent kinetic energy distributions, as shown in Figure 17, with raster plots of Mach number shown for reference. As pointed out by Fletcher et al. [24], instantaneous vorticity concentrations in compressible diffuser flow are highly fragmented, consisting of numerous interlaced vorticity strands of either sense, with high concentrations about domains of large-scale structures that emerge in the time-averaged sense. This is further emphasized in two snapshots of streamwise instantaneous vorticity distributions for the base (Figure 17a) and controlled (Figure 17e) flows, where weaker four-fold accumulations of vorticity concentrations are seen in the controlled flow, compared to two top-and-bottom domains of higher-intensity strands of the base flow (Figure 17a). As the dominant motions of these vorticity clusters (with many other higher modes) are associated with clockwise and counter-clockwise large-scale rotations, the mean vorticity distributions reduce to raster plots in Figure 17b (baseline) and 17f (controlled), as previously shown in Figure 13e-1 and 13e-2. Still, instantaneous flow fields are clearly much more complex, as emphasized in Figures 17a and e. Mach number distributions in Figures 17 c and g closely follow distributions of the mean streamwise velocities that have previously been discussed (Figure 16 a and e), while revealing a bit more nuances. Vortex pairs of the base flow clearly impose significant and expansive blockage to the AIP flow, which, in turn, accelerates the outer flow on the sides, inducing even more nonuniformity across the full AIP face (Figure 17c). Compared to that distribution, the controlled flow (Figure 17g) results in a much more uniform core flow, having the Mach number deficit pushed in elongated near-surface domains. Lastly, a rather dramatic change is seen in the turbulent fluctuations of the flow at the AIP, expressed through the full turbulent kinetic energy TKE. Besides posing a significant flow blockage, vortex pairs of base flow are associated with high levels of TKE (Figure 17d). Along with suppression of these vortex pairs in controlled flow (Figure 17h), TKE levels drop dramatically. It might be somewhat counterintuitive that the introduction of a number of small-scale control vortices upstream, which certainly increase TKE levels locally (as also shown by Fletcher et al. [24]), upon interaction with the diffuser flow would result in a significant reduction of the TKE levels across the full AIP and particularly within its score.

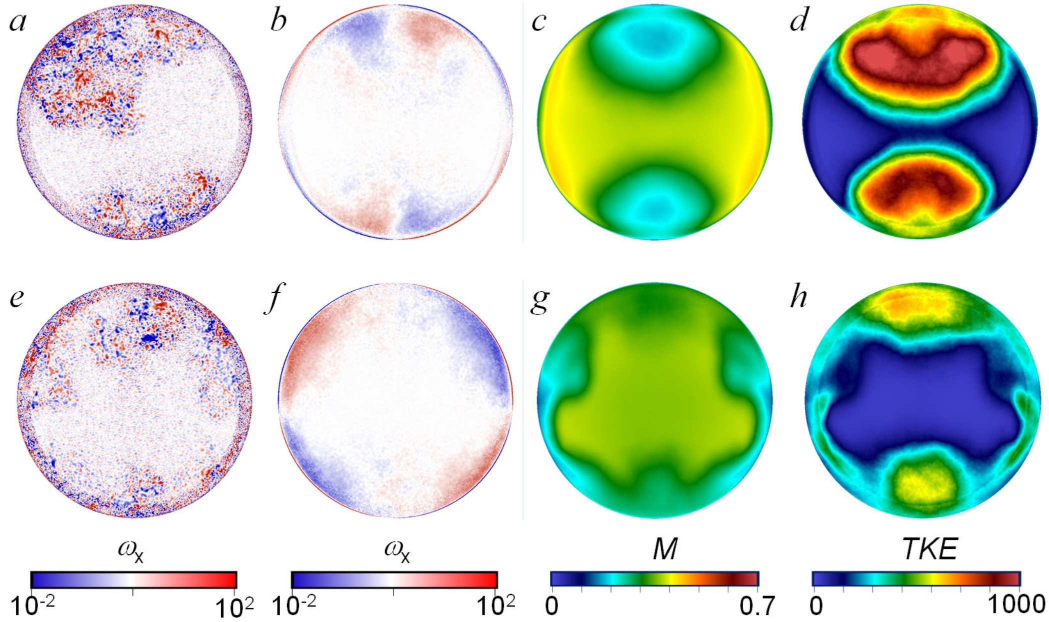

Figure 17. *Color raster plots of the instantaneous (a,e) and time-averaged (b,f) streamwise vorticity, and Mach number (c,g) and turbulent kinetic energy (d,h) at the AIP for the $\theta = 20°$ bend geometry and the upstream $M \approx 0.49$, for the baseline (a–d) and the flow controlled by the top ($C_q = 0.0105$) and bottom ($C_q = 0.0065$) jet arrays (e–h).*

Furthermore, it is noted that the four control-induced large scale vortical structures seen in Figure 17f are actually associated with very low levels of TKE (Figure 17h).

Another important aspect of the total pressure distortion at AIP is related to the aeromechanic impact of distortion patterns on the harmonic excitation of turbine engine inlets. Non-uniform total pressure distribution combined with relative rotor blade motion can create a periodic driving function that results in excitation of the blades. Although total pressure distributions are measured as time-averaged, a procedure was developed for relating nonuniform total pressure distributions across AIP

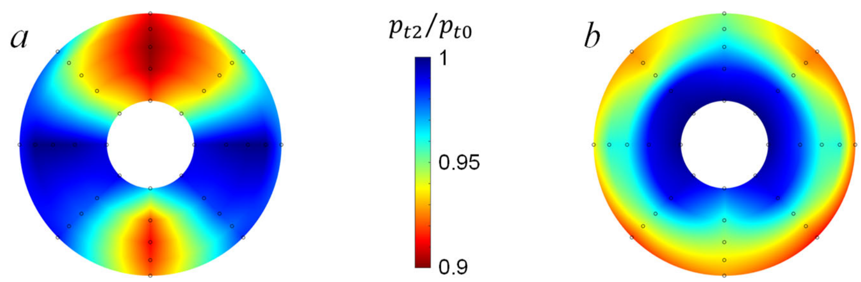

n	1	2	3	4
FOM	0.3465	0.6364	0.1902	0.3872
Ring	1	3	3	5

n	1	2	3	4
FOM	0.1451	0.1035	0.1306	0.2945
Ring	5	4	3	4

Figure 18. *Color raster plots of the AIP time-averaged total pressure for the $\theta = 20°$ bend geometry and the upstream $M \approx 0.49$, for the baseline (a) and the flow controlled by the top ($C_q = 0.0105$) and bottom ($C_q = 0.0065$) jet arrays (b), with the corresponding tables for the aeromechanical excitation figures of merit (FOM) for the first four indices n.*

rakes to different orders of excitation n, as outlined in SAE APR6912 [32]. The process involves Fourier series decomposition of individual rake rings and utilization of Fourier coefficients for defining the 'forcing magnitude'. Next, the Harmonic Excitation Index (HEI) is defined by normalizing those forcing magnitudes by the face-averaged velocity head per ring and for each excitation order n. Finally, the 'figure of merit' FOM for each excitation order n is found as the maximum HEI across all rings.

The above-outlined procedure is conducted for the baseline and the controlled flow with the bend (θ = 20°, r/D = 0.35) that results in the minimized $DPCP_{\mathrm{avg}}$ distortion ($C_{\mathrm{q,inner}}$ = 0.0105, $C_{\mathrm{q,outer}}$ = 0.0065), and the corresponding raster plots of the AIP total pressure distributions are shown in Figures 18a and b, respectively. It is not surprising that the axisymmetric redistribution of the total pressure of the controlled flow results in less azimuthal total pressure variation and hence reflects in lesser excitation of the blades. Therefore, as seen in the tables below, for each of the contour plots, excitation indices decrease across all four excitation orders n, while also shifting the peak excitation away from the surface. While this analysis indicates a generally positive effect of flow control on all possible excitations, judging the full benefit would be engine-specific and would need to be evaluated based on the application.

VII. Conclusions

Controlled suppression of streamwise vortices that form within aggressive diffusers of compact propulsion inlet systems by fluidic actuation was investigated numerically and experimentally. The evolution of these vortices is marked by losses in pressure recovery and significant distortion in distributions of total pressure at the AIP with potential adverse aeromechanical effects. As shown in the present and earlier works by the authors, such vortices can be independently induced by secondary flows associated with Dean circulations in diffuser bends or by internal, confined flow separation owing to local adverse streamwise pressure gradient. The earlier works by Fletcher et al. [24] and Li et al. [25] followed the evolution of a single counter-rotating vortex pair that forms within the diffuser bend in the absence of internal separation to the AIP and demonstrated their mitigation by fluidic actuation. Spanwise arrays of surface jets along the inner bend surface that are asymmetrically yawed about the bend's center plane throttled the transport of streamwise vorticity to the vortex cores and significantly altered their effects on the distribution of total pressure at the AIP, leading to a significant reduction in distortion (up to 60%). It is noted that the concave (outer) surface of the bend also gives rise to Görtler vortices [31], but they typically do not evolve into larger scale streamwise vortices at the AIP. The present investigations focused on the effects of flow separation along each of the symmetrically diverging surfaces of an aggressive high aspect ratio (AR = 6) rectangular to circular diffuser section on the formation of a counter-rotating streamwise vortex pair associated with the separation on each surface. The diffuser was installed upstream of the inlet system AIP and the evolution of the separation-induced vortices was investigated in the presence and absence of a bend section upstream of the diffuser. The present investigations showed that in the absence of the bend, flow separation on each diverging surface of the diffuser led to the formation of a counter rotating vortex pair and that the two pairs were nominally symmetric about the center plane normal to the short sides of the rectangular diffuser inlet. This indicates (as also shown in the work of Burrows et al. [21]) that the contraction and deflection of the core flow over the separated domain results in folding of oncoming concentrations of spanwise vorticity in the boundary layers into a vortex pair. In the presence of an upstream bend, the two vortex pairs are no longer symmetric and the pair that is downstream of the inner surface of the bend is stronger as a result of the additional bend vortices. The presence of these vortex pairs and the changes in their symmetry was clearly reflected in distributions of the total pressure at the AIP. Therefore, the present investigations demonstrated two separate flow mechanisms that induce counter-rotating streamwise vortex pairs within the diffuser having similar AIP topologies.

In the present investigations the control approach of the bend streamwise vortices introduced by Fletcher et al. [24] and Li et al. [25] was extended to explore the mitigation of the two pairs of streamwise vortices by using similar spanwise arrays of surface jets that are placed upstream along each of the long sides of the diffuser's inlet and are asymmetrically yawed about the inlet's center plane. It is noted that this approach is rooted in and places emphasis on control of the evolution of the secondary vortices rather than conventional suppression of the internal flow separation. Similar to the control mechanism described by Fletcher et al. [24], the control surface jets give rise to surface-bound streamwise vortices having a respective opposite sense to each of the vortices of the forming streamwise vortex pair. It was shown that initially the surface-bound control vortices formed by the yawed jets interact destructively with concentrations of opposite sense vortices in the base flow and suppress accumulation of streamwise vorticity of the base flow. However, subsequent coalescence of control-induced vortices into larger scale vorticity concentrations, counter rotating on the sides of the diffuser's center plane, advects near-surface flow away from the central plane and cut off the surface vorticity that would feed the vortex pairs of the base flow. It is remarkable that while the actuation did not lead to significant re-attachment of the separated base flow, its cumulative effect on the vortex-induced flow led to cross-stream spreading of the core flow, inducing a reasonably axisymmetric distribution of the total pressure at the AIP albeit with some azimuthal deficit near the AIP's surface. The axial symmetry of the total pressure distribution at the AIP led to a reduction of 50-70% in the circumferential total pressure distortion parameter $DPCP_{\text{avg}}$, although the inherent radial stratification of the total pressure had a detrimental effect on the maximum radial distortion $DPRP_{\text{max}}$, which was almost negligible in the base flow. A noted benefit of the controlled axisymmetric pattern of total pressure was observed in connection with aeromechanics in the controlled flow, where all excitation indices up to the fourth relevant order were significantly reduced.

Acknowledgment/Disclaimer

This work was sponsored by the Office of Naval Research (ONR), under grant number N000142312500. The views and conclusions contained herein are those of the authors only and should not be interpreted as representing those of ONR, the U.S. Navy, or the U.S. Government. The authors acknowledge the computational resources provided by the Department of Defense (DoD) High Performance Computing Modernization Program, specifically the DoD ERDC and Navy DoD Supercomputing Resource Center systems.

References

[1] Connolly, B.J., Loth, E., Smith, C.F., "Unsteady Flow Simulations for Diffusing S-ducts of Circular and Rectangular Cross-section," AIAA Paper 2018-2130, 2018.

[2] Dean, W.R. "Note on the Motion of Fluid in a Curved Pipe," Philosophical Magazine*,* Vol. 4, 1927, pp. 208-223.

[3] Stahl, S. L., Gaitonde, D. V., Powers, R., Spyropoulos, J.T., "Modal Analysis of Serpentine Diffuser Distortion," AIAA Paper 2023-3308. 2023.

[4] Sandeep, E. J., Liwei, Z., and Frank, K. L., "Flow Separation Control and Drag Reduction in an

Asymmetric Diffuser Using Vortex Generators," AIAA Paper 2022-1067. 2022.

[5] Burrows, T. J., Vukasinovic, and Glezer, A., "Control of a Transonic Shock in a Serpentine Diffuser using Surface Fluidic Actuation," AIAA Paper 2019-3687. 2019.

[6] Hall, G., Hurwitz, W., Tiebens, G., Norby, W., Singshinsuk, P., and Wilt, C., “Development of the F/A-18 E/F Air Induction System,” AIAA Paper 93-2152, 1993.

[7] Anderson, B. H., and Gibb, J., “Study on Vortex Generator Flow Control for the Management of Inlet Distortion,” Journal of Propulsion and Power, Vol. 9, 1993, pp. 422–430.

[8] Owens, L. R., Allan, B. G., and Gorton, S. A., “Boundary-Layer-Ingesting Inlet Flow Control,” Journal of Aircraft, Vol. 45, 2008, pp. 1431–1440.

[9] Tanguy, G., MacManus, D. G., Zachos, P., Gil-Prieto, D., and Garnier, E., “Passive Flow Control Study in an S-Duct Using Stereo Particle Image Velocimetry,” AIAA Journal, Vol. 55, No. 6, 2017, pp. 1862–1877.

[10] Scribben, A., Ng, W., and Burdisso, R., “Effectiveness of a Serpentine Inlet Duct Flow Control Technique at Design and Off-Design Simulated Flight Conditions,” Journal of Turbomachinery, Vol. 128, No. 2, 2006, pp. 332–339.

[11] Anderson, B. H., Miller, D. N., Addington, G. A., and Agrell, J., “Optimal Micro-Jet Flow Control for Compact Air Vehicle Inlets,” NASA/TM—2004-212937, 2004.

[12] Gartner, J., and Amitay, M., “Flow Control in a Diffuser at Transonic Conditions,” AIAA Paper 2015-2484, 2015.

[13] Rabe, A., “Effectiveness of a Serpentine Inlet Duct Flow Control Scheme at Design and Off-design Simulated Flight Conditions,” Ph.D. Thesis, Virginia Tech, 2003.

[14] Harrison, N., Anderson, J., Fleming, J., and Ng, W., “Active Flow Control of a Boundary Layer-Ingesting Serpentine Inlet Diffuser,” Journal of Aircraft, Vol. 50, No. 1, 2013, pp. 262–271.

[15] Garnier, E., “Flow Control by Pulsed Jet in a Curved S-Duct: A Spectral Analysis,” AIAA Journal, Vol. 53, No. 10, 2015, pp. 2813–2827.

[16] Salazar, J. A. P., Goel, A., Costich, R., Koca, M., Tumuklu, O., and Amitay, M. "Data-Driven Pressure Recovery Regulation in Diffusers," AIAA Paper 2026-1137, 2026.

[17] Amitay, M., Pitt, D., and Glezer, A., “Separation Control in Duct Flows,” Journal of Aircraft, Vol. 39, No. 4, 2002, pp. 616–620.

[18] Mathis, R., Duke, D., Kitsios, V., and Soria, J., “Use of Zero-net-mass-flow for Separation Control in Diffusing S-duct,” Experimental Thermal and Fluid Science, Vol. 33, No. 1, 2008, pp. 169–172.

[19] Gissen, A. N., Vukasinovic, B., McMillan, M. L., and Glezer, A., “Distortion Management in a Boundary Layer Ingestion Inlet Diffuser Using Hybrid Flow Control,” Journal of Propulsion and Power, Vol. 30, No. 3, 2014, pp. 834–844.

[20] Burrows, T. J., Vukasinovic, B., Lakebrink, M. T., Mani, M., and Glezer, A., “Control of Flow Distortion in Offset Diffusers using Trapped Vorticity,” International Journal of Heat and Fluid Flow, Vol. 75, 2019, pp. 122–134.

[21] Burrows, T. J., Vukasinovic, B., Glezer, A., Lakebrink, M. T., and Mani, M., “Experimental and Numerical Investigation of Active Flow Control of a Serpentine Diffuser,” AIAA Journal, Vol. 59, 2021, pp. 607–620.

[22] Burrows, T. J., Vukasinovic, B., Glezer, A., Lakebrink, M. T., and Mani, M., “Controlled Flow in a Serpentine Diffuser with a Cowl Inlet,” Journal of Aircraft, Vol. 62, 2025, pp. 438 – 447.

[23] Stratton, Z., Spyropoulos, J.T., Mani, M., Mace, J., Li, S., Fletcher, J., Vukasinovic, B., and Glezer, A., “Development of an Aggressive Offset Diffuser Testbed with Adaptive Design Characteristics”, AIAA Paper 2025-2108, 2025.

[24] Fletcher, J., Li, S., Vukasinovic, B., Mace, J., Glezer, A., Mani, M., Stratton, Z., and Spyropoulos, J. T., “Fluidic Control of the Flow within a Diffuser with Variable Bend,” AIAA Paper 2026-0287, 2026.

[25] Li, S., Fletcher, J., Vukasinovic, B., Mace, J., Glezer,A., Mani, M., Stratton, Z., and Spyropoulos, J.T., “Control of Flow Circulations in a Programmable Offset Diffuser”, AIAA Paper 2025-3392, 2025.

[26] Society of Automotive Engineers Inc., “Gas Turbine Engine Inlet Flow Distortion Guidelines,” 2017. ARP 1420 Rev. C.

[27] Ham, F., Mattsson, K., and Iaccarino, G., “Accurate and Stable Finite Volume Operators for Unstructured Flow Solvers,” CTR Annual Research Briefs, 2006, pp. 243–261.

[28] Bres, G. A., Bose, S. T., Emory, M., Ham, F. E., Schmidt, O. T., Rigas, G., and Colonius, T., “Large-Eddy Simulations of Co-annular Turbulent Jet Using a Voronoi-Based Mesh Generation Framework,” AIAA Paper 2018-3302, 2017.

[29] Kawai, S., and Larsson, J., “Wall-Modeling in Large-Eddy Simulation: Length Scales, Grid Resolution, and Accuracy,” CTR Annual Research Briefs, 2010, pp. 39–46.

[30] Germano, M., Piomelli, U., Moin, P., and Cabot, W. H., “A Dynamic Subgrid-Scale Eddy Viscosity Model,” Physics of Fluids A - Fluid Dynamics, Vol. 3, 1991, pp. 1760–1765.

[31] Saric, W. S., “Görtler Vortices,” Annual Review of Fluid Mechanics, Vol.26, 1994, pp. 379–409.

[32] Society of Automotive Engineers Inc., “Substantiation of Power Available and Inlet Distortion Compliance for Rotorcraft Engine Inlet Barrier Filter Installations,” 2023. ARP 6912.